FTLE Computation Beyond First-Order Approximation

Markus Üffinger[1], Filip Sadlo[1], Mike Kirby[2], Charles Hansen[2] and Thomas Ertl[1]

[1] Visualization Research Center Universität Stuttgart (VISUS), Germany
[2] Scientific Computing and Imaging Institute, University of Utah

Abstract

We present a framework for different approaches to finite-time Lyapunov exponent (FTLE) computation for 2D vector fields, based on the advection of seeding circles. On the one hand it unifies the popular flow map approach with techniques based on the evaluation of distinguished trajectories, such as renormalization. On the other hand it allows for the exploration of their order of approximation (first-order approximation representing the flow map gradient). Using this framework, we derive a measure for nonlinearity of the flow map, that brings us to the definition of a new FTLE approach. We also show how the nonlinearity measure can be used as a criterion for flow map refinement for more accurate FTLE computation, and we demonstrate that ridge extraction in supersampled FTLE leads to superior ridge quality.

Categories and Subject Descriptors (according to ACM CCS): I.3.8 [Computer Graphics]: Applications Physical Sciences and Engineering—

1. Introduction and Motivation

The *finite-time Lyapunov exponent* (FTLE) is a measure of separation in instationary vector fields. It is used to reveal the overall structure of the vector field: FTLE *ridges* (its generalized local maxima) indicate strong separation, and separate different regions with coherent flow behavior. There are several approaches for computing FTLE fields. They share the basic approach of integrating *trajectories* for a given time T and measuring the separation with respect to their end points. When advection time T is increased, separation is typically subject to exponential growth, resulting in highly complex FTLE fields, which typically exhibit a very fine, folded ridge structure. Thus, appropriate sampling of FTLE fields can become a computationally infeasible challenge in practice, as the resolution of the FTLE sampling cannot be increased arbitrarily. This results in aliasing artifacts in the computed FTLE fields due to undersampling that, among other, hinders robust ridge extraction. There are techniques that calculate FTLE accurately at given sample locations by locally decreasing the sampling distance [Nes89, KPH*09]. However, these are prone to missing features, as discussed in Section 2. On the other hand, the popular flow map-based FTLE approach [Hal01] captures those features but is usually limited in the sampling resolution, and thus introduces an error by employing a linearization of the potentially nonlinear separation behavior of the vector field.

In Section 2 we introduce a framework based on seeding circles for the different FTLE approaches. Within this framework we present in Section 3:

- MD-FTLE, a FTLE approach which accounts for nonlinearity, is based on the flow map to avoid missed features, and reduces aliasing.
- A measure to quantify nonlinearity that can serve as an indicator for undersampling and is used as a refinement criterion for adaptive FTLE computation [GGTH07, SP07, AGJ11] in Section 4.
- Circumference FTLE (C-FTLE), which measures nonlinear deformation of the seeding circles.
- FTLE supersampling which reduces ridge extraction artifacts due to aliasing (Section 4).

Note, the advantage of supersampling was demonstrated for hyperbolicity time fields [SW10], which, as an alternative to ridges from FTLE, can be used to obtain *Lagragian coherent structures* (LCS). We investigate our techniques with a CFD result of buoyant air flow in a container heated at the bottom and cooled at the top. For our evaluation we chose a region of interest (ROI) with prominent FTLE ridge structures.

2. Framework for FTLE Computation

The Lyapunov exponent (LE) is used to study the rate of separation of infinitesimally close trajectories in a temporally

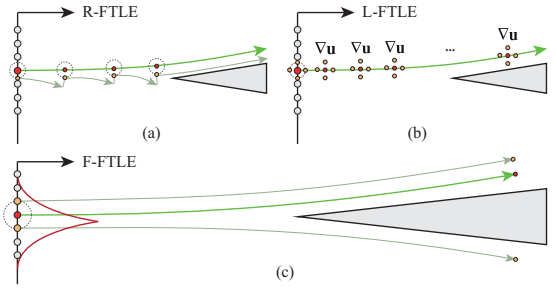

Figure 1: *R-FTLE (a) and L-FTLE (b) are prone to missing separation, e.g., FTLE ridges, due to local measurement of flow stretching. F-FTLE in contrast captures the ridge (c).*

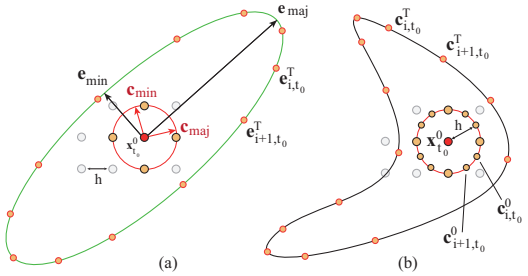

Figure 2: *F-FTLE approximates the flow map linearly, e.g., by $\nabla\phi^T_{t_0}$ derived from four seeding trajectories (a). Using more seeds on the circle captures the nonlinear behavior of $\phi^T_{t_0}$ (b). Here, both, the linear separation ellipse in (a) (green) and the deformed seed circle after advection for time T in (b) (black) are drawn at their seed location $\mathbf{x}^0_{t_0}$.*

unconstrained system. The largest LE $\sigma_1(\mathbf{x})$ is defined as

$$\sigma_1(\mathbf{x}) = \lim_{T\to\infty} \lim_{\|\delta(\mathbf{x},t_0)\|\to 0} \frac{1}{|T|} \ln \frac{\|\delta(\mathbf{x},t_0+T)\|}{\|\delta(\mathbf{x},t_0)\|}, \qquad (1)$$

where $\delta(\mathbf{x},t) = \delta^t_{t_0}$ is a perturbation at time t, having originated at position $\mathbf{x}$ and time t_0, and oriented at time t_0 such that σ_1 becomes maximal. The FTLE examines a finite time interval $[t_0, t_0+T]$ in contrast to $T\to\infty$, hence the separation, or predictability, of trajectories after time T.

One class of approaches for evaluating (1) are based on renormalization [Nes89], using differently oriented pairs of trajectories. Thereby the reference trajectory is seeded at $\mathbf{x}$ and the other on a circle with radius h (Figure 1 (a)). The latter trajectory is kept close to the reference by renormalization, i.e., by projecting it toward the reference trajectory. The overall separation is accumulated over the renormalization steps, yielding the FTLE value (R-FTLE) at point $\mathbf{x}$.

A second class of approaches, e.g., the localized FTLE (L-FTLE) [KPH*09], accumulate information from the velocity gradient along the trajectory starting at $\mathbf{x}$ (Figure 1 (b)).

An alternative approach (F-FTLE) to compute the FTLE was made popular by Haller [Hal01]. It is based on the *flow map* $\phi^T_{t_0}$, which maps seed points $\mathbf{x}^0_{t_0}$ of trajectories started at t_0 to their respective end points $\phi^T_{t_0}(\mathbf{x}^0_{t_0}) = \mathbf{x}^T_{t_0}$ after advection for time T (Figure 1 (c)). The largest FTLE is obtained as

$$\sigma^T_{f,t_0} = \frac{1}{|T|} \ln \sqrt{\lambda_{\max}\left((\nabla\phi^T_{t_0})^\top \nabla\phi^T_{t_0}\right)} \qquad (2)$$

with $\lambda_{\max}(\cdot)$ being the major eigenvalue. Note that this represents a first-order approximation of $\phi^T_{t_0}$ based on $\nabla\phi^T_{t_0}$. In practice, $\phi^T_{t_0}$ is discretized on a grid with cell size h leading to a linearization error depending on h. Since this approach is based on the gradient of neighboring flow map samples, the detection of separation is continuous, i.e., no separation can be missed due to "holes" in the sampling. As illustrated in Figure 1 this ensures that FTLE ridges, which are of great interest for topological flow analysis, are not missed. R-FTLE and L-FTLE, in contrast, may miss such features. On the other hand, they have the advantage that L-FTLE provides, up to numerics, accurate FTLE values, and R-FTLE converges toward those as $h\to 0$. This allows for increasing accuracy without the need to increment the sample number, i.e., increasing flow map resolution.

The motivation for the present paper is the reduction of the linearization error in (2). To this end, we introduce a framework based on seeding circles that serves as a basis for our techniques in Section 3. Within this framework, R-FTLE corresponds to a single sample on the circle and repeated seeding along the reference trajectory, L-FTLE to the limit case $h\to 0$ and continuous seeding, and F-FTLE to four axis-aligned samples on the seeding circle with h identical to the flow map resolution (see Figure 2).

3. Nonlinear FTLE

To combine the suitability for topological analysis of the F-FTLE (its absence of "sampling holes") with better predictability (higher accuracy of FTLE values) of the R-FTLE and L-FTLE approaches, we introduce *multi-directional FTLE* (MD-FTLE). In our framework, it is formulated by a seeding circle radius h identical to the FTLE sampling distance, as in the F-FTLE case, but with additional samples on the circle (Figure 2 (b)). The MD-FTLE is directly obtained from the geometry of the advected circle, conforming to (1), by the maximum distance between the advected circle points $\mathbf{c}^T_{i,t_0}$ and the end point of the reference trajectory $\mathbf{x}^T_{t_0}$:

$$\sigma^T_{md,t_0} = \frac{1}{|T|} \ln\left(\max_{i=1\ldots N}(|\mathbf{c}^T_{i,t_0} - \mathbf{x}^T_{t_0}|/h)\right). \qquad (3)$$

Compared to the popular F-FTLE, our MD-FTLE exhibits a more isotropic evaluation. This leads to a more appropriate sampling with less angular aliasing, i.e., to a reduced sensitivity with respect to the orientation of the initial perturbations, especially in FTLE valleys (Figure 4 (a), (b)). In our experiments, $N > 32$ did not improve the results. Note that MD-FTLE with $N = 4$ is identical to F-FTLE, and that MD-FTLE, as F-FTLE, converges to exact values as $h\to 0$.

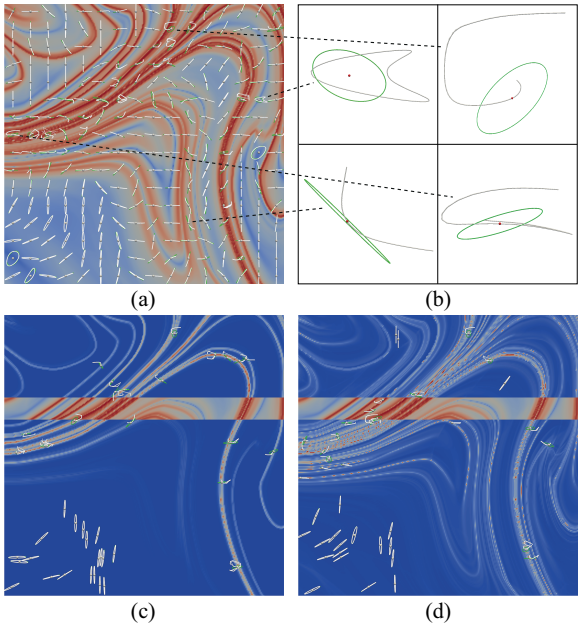

Figure 3: *Nonlinear flow map behavior. (a) F-FTLE σ^T_{f,t_0} with advected seed circles (white) and corresponding linear approximation ellipses (green), both normalized in size, placed at their $\mathbf{x}^0_{t_0}$ (grey). (b) Close-up of four advected seed circles. (c) Linearization error field D with advected circles for a random subset of the 10 percent of samples with highest and lowest error. (d) Same with normalized field, $\bar{D}$. ROI flow map resolution= 256^2, $t_0 = 8.05$, $T = 0.75$.*

Figure 3 (a) shows several advected circles (white) placed at their start locations $\mathbf{x}^0_{t_0}$ and normalized in size. It can be observed that in some regions the circle is deformed linearly to the shape of an ellipse, but in others in a nonlinear manner. The advected circle shapes reveal the true, potentially nonlinear separation behavior of the flow. The traditional F-FTLE approach with its finite resolution, in contrast, is only exact as long as the investigated scale exhibits linear behavior—as long as the circles are deformed to ellipses, e.g., in the lower left quadrant of the field. As illustrated in Figure 3 (b) this linear approximation of the separation

$$\delta^T_{t_0} = (\nabla\phi^T_{t_0})\delta^0_{t_0} + G(\mathbf{x}, \delta^0_{t_0}) \tag{4}$$

using only the flow map gradient $\nabla\phi^T_{t_0}$ can lead to substantial nonlinear error terms G, e.g., visible near the ridges. Increasing the flow map resolution to allow for linearization is typically not feasible due to constraints on computation time and space, especially with larger advection times T and the resulting strong nonlinear deformations. Note, that incorporating G in the computation of $\delta^0_{t_0,\max}$, leading to maximum separation $\delta^T_{t_0}$, is difficult, also in terms of numerics.

Instead, we quantify the strength of the nonlinear deformation geometrically. We measure the deviation of the advected circle to the ellipse representing the linear approximation $\tilde{\delta}^T_{t_0} = (\nabla\phi^T_{t_0})\delta^0_{t_0}$. The major axis $\mathbf{e}_{\text{maj}}$ of the linear approximation is obtained as $h\sqrt{\lambda_{\max}(C)}\varepsilon_{\text{maj}}(C)$, with $\varepsilon_{\text{maj}}(C)$ being the major eigenvector of the right Cauchy-Green tensor $C = (\nabla\phi^T_{t_0})^\top \nabla\phi^T_{t_0}$, and $\mathbf{e}_{\min}$ correspondingly using $\varepsilon_{\min}(C)$ (Figure 2 (a)). Figure 3 (a), (b) show the advected circles (white) together with their linear approximation ellipses (green). To ease visual comparison and the discussion below, both ellipse and advected circle are placed at the FTLE sampling points $\mathbf{x}^0_{t_0}$ (the actual advected circle points $\mathbf{c}^T_{t_0}$ are therefore translated by $\mathbf{x}^0_{t_0} - \mathbf{x}^T_{t_0}$). To evaluate the nonlinearity, we establish a point-wise correspondence between advected circle points $\mathbf{c}^T_{i,t_0}$ and ellipse points $\mathbf{e}^T_{i,t_0}$, using $\mathbf{e}^T_{i,t_0} = \mathbf{x}^T_{t_0} + \nabla\phi^T_{t_0}(\mathbf{c}^0_{i,t_0} - \mathbf{x}^0_{t_0})$. As illustrated in Figure 2 this does not assure an even distribution of $\mathbf{e}^T_{i,t_0}$ on the ellipse. We provide a non-uniform seeding of $\mathbf{c}^0_{i,t_0}$ to still achieve it. To avoid inverting $\nabla\phi^T_{t_0}$, we enforce a denser seeding on the circle in $\mathbf{c}_{\min}$ direction, with $\mathbf{c}_{\min} = (\nabla\phi^T_{t_0})\varepsilon_{\min}(\bar{C})$ being the vector on the seed circle that transforms to the minor axis $\mathbf{e}_{\min}$ of the ellipse, and $\bar{C} = \nabla\phi^T_{t_0}(\nabla\phi^T_{t_0})^\top$ the left Cauchy-Green tensor. The deviation of the advected circle from its corresponding ellipse is obtained as

$$D = 1/N \sum_{i=1..N} |\mathbf{c}^T_{i,t_0} - \mathbf{e}^T_{i,t_0}|. \tag{5}$$

This measure directly reflects the absolute error due to the linear approximation of the flow map. We also define $\bar{D} = D/|\mathbf{e}_{\text{maj}}|$ the linearization error normalized by the maximum separation factor. Figure 3 (c), (d) show resulting fields. The linearization error $D(\mathbf{x})$ reveals regions with high error of F-FTLE, which in particular includes regions with sharp features, e.g., ridges. Hence, it lends itself to be used as a criterion for adaptive refinement of the flow map until the linear

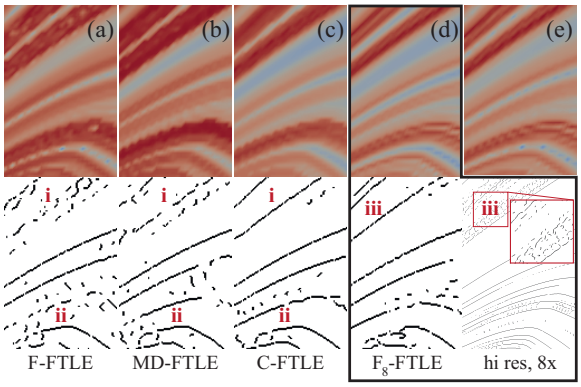

Figure 4: *FTLE and extracted ridges for all approaches: (a) F-FTLE. MD-FTLE (b) and C-FTLE (c) enable more robust ridge extraction, see i and ii. (d) Ridge extraction in 8× brute force supersampled F_8-FTLE performs better than ridge extraction in the 8× hi res field in regions with strong aliasing, see iii. (e) 8× adaptively supersampled F-FTLE. Crop of ROI, 42×27, $N = 32$, $t_0 = 8.05$, $T = 1.0$.*

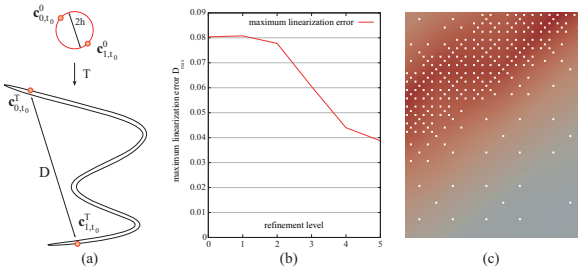

Figure 5: *(a) Nonlinear stretching of the seeding circle. (b) Maximum linearization error $D_{\max}$ for 5 iterations. (c) Refinement hierarchy close-up: criterion D adapts toward ridges (red), which are typically under-resolved.*

flow map approximation is sufficiently well fulfilled. Note, to conserve the "absence of holes" we do not simply reduce the seeding circle radius without increasing the flow map resolution. The normalized error field $\bar{D}(\mathbf{x})$, in contrast, explicitly highlights regions with strongly nonlinear behavior. Interestingly, those are, in our example, not the ridges, but the valleys, the generalized local minima of the FTLE field. The observations made from $\bar{D}$ motivate the definition of circumference FTLE (C-FTLE)

$$\sigma^T_{c,t_0} = \frac{1}{|T|}\ln(\frac{c}{4h}), \tag{6}$$

with c being the circumference of the advected circle. The nonlinear deformation of the seed circle (Figure 5 (a)) also implies that the traditional FTLE (measuring the deformation D by the Euclidean distance) underestimates the total stretching of the initial fluid element. The total stretching rather corresponds to the length of the resulting curve, representing a "Lagrangian distance" instead. Note, that σ^T_{c,t_0} is identical to σ^T_{f,t_0} in the limit case of $h \to 0$ (leading to elliptical transformation) and sufficiently strong separation (leading to ellipses with high eccentricity). Figure 4 (c) shows that aliasing is even more reduced than with σ^T_{md,t_0}.

4. Adaptive Refinement and Supersampling

We implemented a simple refinement scheme to demonstrate the suitability of D to detect undersampling of the FTLE. We start with a regular grid sampling on the coarsest level with each FTLE sample $\sigma^T_{t_0}(\mathbf{x}_{0,i})$ covering the area of one pixel. A sample i on level n at location $\mathbf{x}_{n,i}$ is refined into five subsamples if $D(\mathbf{x}_{n,i})$ is larger than a prescribed threshold. For consistency reasons we keep the original sample location $\mathbf{x}_{n,i}$ and distribute the other four samples uniformly within its cover, see Figure 5 (c). Starting with the same configuration as in Figure 3, but $T = 0.5$ to ease illustration, we performed five refinement iterations to compute the refinement hierarchy for σ^T_{f,t_0}. An overall decrease in the maximum linearization error $D_{\max}$ of all samples of a hierarchy level can be observed (Figure 5 (b)), simultaneously the refinement adapts toward the ridges (c). Note, for heavily undersampled FTLE, $D_{\max}$ can initially show an increase during refinement. To obtain supersampled FTLE fields of the initial flow map resolution we downsample the hierarchy, weighting the FTLE samples according to their covered area. Figure 4 (e) shows $8\times$ adaptively supersampled F-FTLE obtained after 3 refinement iterations. It looks similar to brute-force supersampled F_8-FTLE (the reference) in ridge regions (d), and substantially outperforms F-FTLE (a), justifying the additional expense. The ridges also exhibit more noise in (a) and in regions with strong aliasing the ridges from F_8-FTLE are superior to ridges from F-FTLE with $8\times$ resolution (d),(iii).

5. Conclusion

We presented a framework for FTLE computation based on the advection of seed circles. Within this framework we discussed the limitations of localized FTLE approaches with respect to capturing FTLE ridges and demonstrated the accuracy limitations of the popular F-FTLE approach due to its linear approximation of the flow map. To capture nonlinear separation effects we introduce MD-FTLE that uses many samples on the seed circle and provide a measure for the nonlinear deviation from F-FTLE. The obtained distance metrics gave us new insight and led to the definition of C-FTLE based on the circumference of the advected seed circles which produces results with less aliasing. The linearization error was also used as a refinement criterion for an adaptive FTLE refinement scheme, and we demonstrated that extracting ridges from supersampled FTLE fields is more robust. Our research opens new interesting questions, e.g., concerning the different deformation behavior on ridges and in valleys. In the future we would like to further investigate the properties of our FTLE approach based on nonlinearity.

References

[AGJ11] AGRANOVSKY A., GARTH C., JOY K. I.: Extracting flow structures using sparse particles. In *Vision, Modeling, and Visualization* (2011), pp. 153–160. 1

[GGTH07] GARTH C., GERHARDT F., TRICOCHE X., HAGEN H.: Efficient computation and visualization of coherent structures in fluid flow applications. *Transactions on Visualization and Computer Graphics 13*, 6 (2007), 1464–71. 1

[Hal01] HALLER G.: Lagrangian structures and the rate of strain in a partition of two-dimensional turbulence. *Physics of Fluids 13*, 11 (2001), 3365. 1, 2

[KPH*09] KASTEN J., PETZ C., HOTZ I., NOACK B., HEGE H.-C.: Localized finite-time Lyapunov exponent for unsteady flow analysis. In *Vision Modeling and Vis.* (2009), pp. 265–274. 1, 2

[Nes89] NESE J.: Quantifying local predictability in phase space. *Physica D: Nonlinear Phenomena 35*, 1-2 (1989), 237–250. 1, 2

[SP07] SADLO F., PEIKERT R.: Efficient visualization of Lagrangian coherent structures by filtered AMR ridge extraction. *Transactions on Visualization and Computer Graphics 13*, 5 (2007), 1456–1463. 1

[SW10] SADLO F., WEISKOPF D.: Time-dependent 2-D vector field topology: An approach inspired by Lagrangian coherent structures. *Computer Graphics Forum 29*, 1 (2010), 88–100. 1